A Fourier processor for partially coherent fields

S. A. WADOOD,[1,2] **B. E. NUSSBAUM,**[1,2,3] **T. D. VISSER,**[1,2,4] **T. G. BROWN,**[1,2] **G. P. AGRAWAL,**[1,2,3] **AND A. N. VAMIVAKAS**[1,2,3,5,*]

[1]*The Institute of Optics, University of Rochester, Rochester, New York 14627, USA*
[2]*Center for Coherence and Quantum Optics, University of Rochester, Rochester, New York 14627, USA*
[3]*Department of Physics and Astronomy, University of Rochester, Rochester, New York 14627, USA*
[4]*Department of Physics and Astronomy, Vrije Universiteit, Amsterdam, NL-1081HV, The Netherlands*
[5]*Materials Science, University of Rochester, Rochester, NY 14627, USA*
[*]*Corresponding author: nick.vamivakas@rochester.edu*

Abstract: We extend conventional coherent Fourier processing techniques to a partially coherent field and modify its spatial coherence using a 4*f* system. The coherence is measured by a modified Mach–Zehnder interferometer. Our results corroborate the predictions in [Opt. Lett. **42**, 4600 (2017)] and can be extended to a more sophisticated processing of spatial coherence.

1. Introduction

Fourier optics is a well established field [1] , starting with the experiments of Abbe [2] and Porter [3] on Fourier processing of coherent optical signals more than a century ago. The extension of Fourier processing techniques to spatially partially coherent light beams is not straightforward, since the image formation is not linear in either the field, as in coherent systems, or in intensity, as in incoherent systems [4]. In this letter we study the effect of a spatial filter in a 4*f* system, which is the canonical optical processor, on the spatial coherence of a light beam. This is quantified by the spectral degree of coherence which is related to the visibility of the fringes formed in a Young's experiment [5]. The theoretical study of this system was carried out in [6]. Even though the synthesis of partial coherence is a mature field of research ([7–11], also see references in [6]), experimental demonstration of Fourier processing of partially coherent fields has received little attention. The works in [12,13] performed a quantitative measurement of the Fourier processing of spatial coherence via a pinhole array mask in the Fourier plane. In this work, we study the Fourier processing of a partially coherent field due to a single pinhole filter in the Fourier plane.

The basic idea of the experiment, as discussed in [6], is illustrated in Fig. (1). A partially coherent input field of frequency ω with the cross-spectral density (CSD) $W_{in}(\boldsymbol{\rho}_1, \boldsymbol{\rho}_2, \omega) = \langle E^*(\boldsymbol{\rho}_1)E(\boldsymbol{\rho}_2)\rangle$, where $\boldsymbol{\rho} = (x, y)$ denotes the transverse coordinates, is incident on a 4*f* system. In what follows, we drop the frequency argument ω for brevity. In the Fourier plane, a pinhole acts as a spatial filter for the CSD. The CSD at the output plane is controlled by the size of this pinhole. Assume that the input field is delta-correlated and has a uniform spectral density S_{in} i.e. $W_{in}(\boldsymbol{\rho}_1, \boldsymbol{\rho}_2) = S_{in}\delta^2(\boldsymbol{\rho}_1 - \boldsymbol{\rho}_2)$, where δ^2 denotes a 2D delta function. If we ignore the finite extent of the lens, the field at the Fourier plane is also delta-correlated and has a uniform spectral density. For a finite lens aperture, the field is Bessel-correlated [6, Eq. (16)]. Assuming the spatial filter is much larger than the coherence area at the Fourier plane, the width of the spatial filter then controls the effective size of an incoherent source, which via the van Cittert–Zernike relation affects the CSD at the output plane [4] . The normalized output CSD, also called the degree of spatial coherence $\mu(\boldsymbol{\rho}_1, \boldsymbol{\rho}_2) = W_{out}(\boldsymbol{\rho}_1, \boldsymbol{\rho}_2)/\sqrt{W_{out}(\boldsymbol{\rho}_1, \boldsymbol{\rho}_1)W_{out}(\boldsymbol{\rho}_2, \boldsymbol{\rho}_2)}$ is plotted in Fig. (1) for $f = 500$ mm, and is given as

$$\mu(\boldsymbol{\rho}_1, \boldsymbol{\rho}_2) = \frac{f}{ka\Delta\boldsymbol{\rho}}J_1\left(\frac{ka\Delta\boldsymbol{\rho}}{f}\right),\tag{1}$$

where a denotes the radius of the pinhole, k is the wavenumber, J_1 is the Bessel function of the first kind of order 1, and $\Delta\rho = |\rho_2 - \rho_1|$. Note that we are assuming a symmetric measurement around the beam axis i.e. $\rho_1 = -\rho_2$, and therefore the degree of spatial coherence is real.
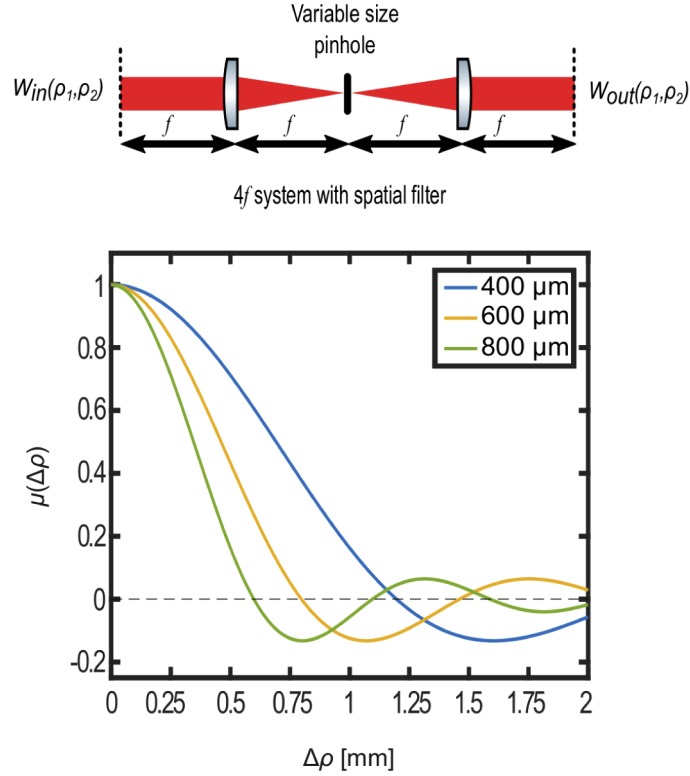

Fig. 1. Fourier Processing of CSD $W(\rho_1, \rho_2)$. Top: A $4f$ system with a variable width pinhole which acts as a spatial filter. The width of the output coherence can be controlled by the size of the spatial filter. Bottom: The degree of spatial coherence is plotted as a function of the radial difference coordinate $\Delta\rho = |\rho_2 - \rho_1|$ for $f = 500$ mm and $\lambda = 785$ nm . The input is assumed to be delta-correlated. Legend indicates the diameter of the pinhole.

2. Experimental setup

To implement the Fourier processing of partial coherence, we use the setup shown in Fig. (2). A collimated, linearly polarized Gaussian beam with CSD W_a of wavelength 785 nm and linewidth 1 MHz (TOPTICA DL 100) impinges on a rotating ground glass diffuser. The diffuser is placed in the front focal plane of a lens, and therefore the size of the laser spot on the diffuser controls the coherence area at the backfocal plane of the lens [4]. The spot size on the diffuser (>1 mm) is such that the coherence area of the beam input to the $4f$ system, with CSD W_b, is very small, i.e., almost delta-correlated. The pinhole controls the coherence area of the output beam. To measure the CSD W_c of the output beam, we use a Mach–Zehnder interferometer with an extra mirror (MZIM) in one arm [14]. One of the arms of the MZIM is tilted and the fringes are observed on the CCD. The path length difference between two arms is approximately 4 inches, which is much less than the coherence length of the laser, which is approximately 100 m. This is one of the many possible schemes for impelementing reverse wavefront interferometry to measure spatial coherence [15–17]. Note that this scheme differs from the noninterferometric technique used in [12,13] which relies on the relationship between the intensity and field correlations for thermal

light sources [5]. One advantage of using reversed wavefront interferometry is that the symmetric coherence function is displayed directly on the CCD. Secondly, since it does not rely on the use of Gaussian field statistics, our setup can also be used to directly measure spatial coherence of non-classical light sources.
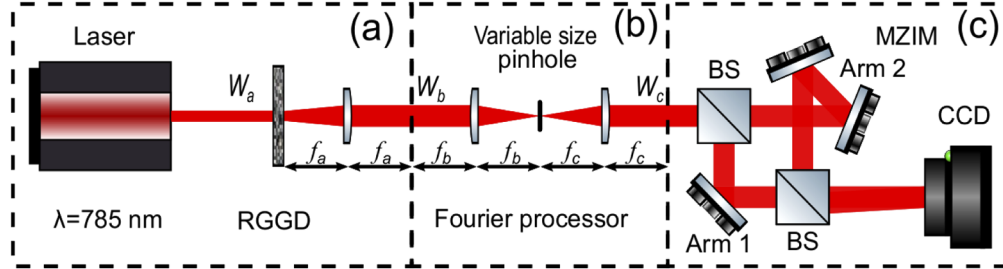

Fig. 2. The experimental setup. a: A linearly polarized Gaussain laser mode with a coherence function W_a impinges on a spinning ground glass diffuser. b: The size of the beam on the ground glass controls the spatial coherence W_b presented to the 4f system. Note that the ground glass is conjugate to the pinhole plane. The size of the pinhole then dictates the spatial coherence W_c of the output field of the Fourier processor. c: To measure the spatial coherence, we use a MZIM in one arm. We add a tilt to one of the arms and observe the tilt fringes on a CCD. RGGD: Rotating Ground Glass Diffuser. BS: beamsplitter, $f_a = 80\,\text{mm}, f_b = 100\,\text{mm}$, and $f_c = 500\,\text{mm}$. The approximate distance from the output of the 4f system to the CCD is 0.9 m .

To align the system, we first keep the ground glass stationary, and observe a spatially coherent speckle pattern on the CCD [18]. For a stationary ground glass the width of the speckle, determined by the intensity autocorrelation of the total speckle pattern, changes with the size of the pinhole in the 4f system. Because the speckle size observed for a stationary ground glass is a proxy for the coherence area of the beam when the ground glass is spinning [19], it is expected that the pinhole affects the spatial coherence of the output beam. After aligning the speckle pattern, we start rotating the ground glass with a motor. The time averaged output intensity or the spectral density at the CCD is

$$
\begin{aligned}
S(x, y) &= \langle |E(x, y)|^2 \rangle + \langle |E(-x, y)|^2 \rangle \\
&+ 2\text{Re}\{\langle E^*(x, y)E(-x, y) \rangle e^{ik_y y}\}, \\
&= S_1(x, y) + S_2(x, y) + 2\text{Re}\{W(x, y, -x, y)e^{ik_y y}\}
\end{aligned}
\tag{2}
$$

where $\langle \ldots \rangle$ denotes time averaging, $S_{1,2}$ are the individual spectral densities due to arms 1,2, $k_y = k\alpha_y$, where α_y is the direction cosine in y direction, and W is the CSD at the CCD plane. The MZIM therefore directly measures the correlations between the points (x, y) and $(-x, y)$. The change in visibility of the horizontal fringes across the x direction on the CCD gives a direct measure of the spatial coherence in the x direction across the beam. The symmetric measurement about the x axis ensures that the measured $W(x, y, -x, y)$ is stationary, which is also expected for the quasihomogenous source formed at the Fourier plane of the 4f system [4]. This is sufficient to demonstrate the Fourier processing of partially coherent fields, without performing the most general measurement of spatial coherence for all pairs of points $(x_1, y_1), (x_2, y_2)$ in the output plane of the 4f system.

A representative image for the 600 μm pinhole is shown in Fig. 3. The image is an average of 250 speckle patterns where each individual speckle pattern was recorded on the CCD with an integration time of 20 ms. We also perform digital filtering of each frame to get rid of fringes due to backreflections and diffraction from dust particles on the CCD slide. The center linecut

corresponds to rays originating from the same point on the wavefront, and thus has the highest amplitude of the horizontal fringe. Progressing either right or left from the center linecut samples the $W(x, -x)$ point of the coherence function. The second linecut corresponds to points which have minimal correlations between them, and correspond to zeros of W. The coherence revives again but with an extra phase of π, which can also be seen by the contrast reversal of the fringes. We can find the visibility of the fringe pattern corresponding to a linecut $S(x)$ in Fig. 3. by using the formula

$$\mathcal{V}(x) = \frac{AC(x)}{DC(x)} = \frac{2\sqrt{S_1(x)S_2(x)}}{S_1(x) + S_2(x)} |\mu(x, -x)|, \tag{3}$$

where $AC(x)$ is the integrated power in the spatial Fourier transform of the linecut $S(x)$, filtered in a narrow bandwidth around the spatial frequency k_y. Similarly, $DC(x)$ is the zero spatial frequency content of the linecut, and is also equal to the spatial integral of the linecut. For a fringe
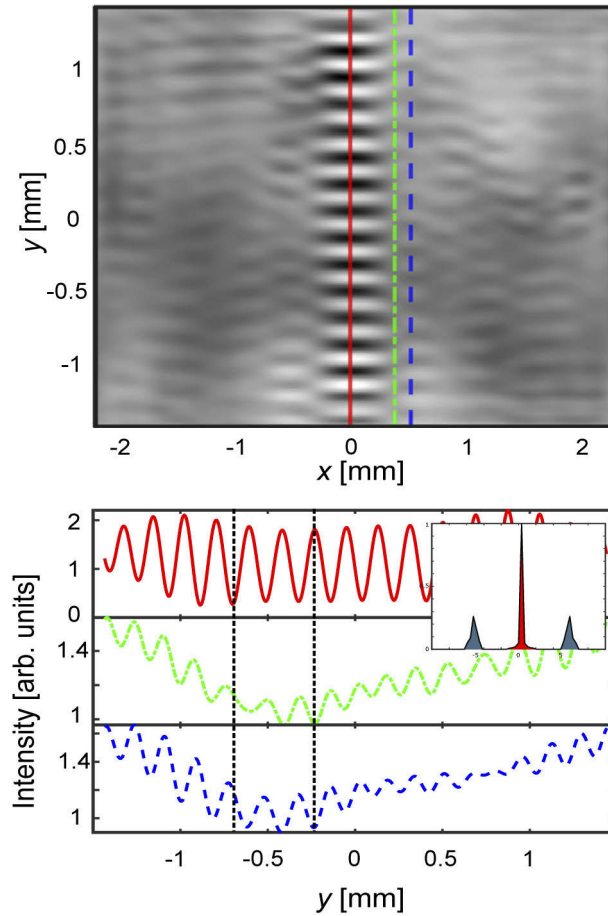

Fig. 3. Top: Horizontal tilt fringes observed at the output of the MZIM. Moving along x direction, the fringe visibility along a column is modulated according to $\mu(x)$, as indicated by the three linecuts. Bottom: Vertical linecuts corresponding to the three lines in the top figure. The inset shows the amplitude of the spatial Fourier transform of the top (solid red) linecut. The visibility given by Eq. (3) corresponds to the ratio of the shaded areas of the sidebands and the central peak. In the bottom figure, the black dashed lines cutting across the three linecuts highlight the contrast reversal of the fringes, indicating a change in the sign of $\mu(x)$.

pattern at a given spatial frequency, Eq. (3) is equivalent to the familiar definition of visibility as $(\max\{S(x)\} - \min\{S(x)\})/(\max\{S(x)\} + \min\{S(x)\})$, where $\max(\min)\{S(x)\}$ is the maximum (minimum) of the intensity linecut at x. Figure (3) shows three such linecuts and spatial Fourier transform of the central fringe. Measuring the visibility using Eq. (3) therefore gives a direct measurement of the magnitude of $\mu(x, -x)$. Note that Fig. (3) does not show uniform intensity, as would be expected of a uniformly illuminated RGGD. This is because we are measuring field correlations and not intensities, and Fig. (3) shows how the tilt phase at a point in an ensemble of speckle fields becomes less correlated with points farther than the coherence area. The slowly varying envelope on the linecuts in Fig. (3) can be attributed to the digital filtering to clean the individual speckle images in the Fourier domain.

3. Results

Figure (4), which is the main result of this paper, shows the experimentally measured visibility of the horizontal fringes as a function of the horizontal direction for different pinhole sizes. For each point in x, the visibility for the linecut in y is calculated using Eq. (3). The visibilities are normalized by the central fringe visibility. We use the width of the central lobe, which is determined by the distance between the global maximum and the first zero of the coherence function, as a measure of the coherence area. The choice of this measure is subjective, and other measures such as full width at half maximum can also be used. For the 400 μm pinhole, the first zero of the coherence function is at $\Delta x = 1128$ μm. The coherence area almost halves for the 800 μm pinhole, with the first zero at $\Delta x = 588$ μm. The dashed lines in Fig. (4) correspond to the expected coherence functions as predicted by Eq. (1). Even though Eq. (1) is valid for an infinite lens aperture and the observation plane at the output of the 4f system, and not at the CCD plane, there is good agreement between the theory predictions shown in Fig. (1) and the experimental results of Fig. (4). Qualitatively, this is expected if the fields represented by W_b and W_c are collimated. Then, W_c will not change significantly upon propagation from the output of the 4f through the MZIM to the CCD plane. Mathematically, the fact that the coherence function changes very slowly upon propagation through the MZIM is related to the large Fresnel number ($N_F \approx 142$) associated with the last lens of the 4f system and beam propagation from the output of the 4f through the MZIM to the CCD. We have also confirmed this with a simulation using the Coherent Mode Decomposition (CMD) [20]. The grey lines in Fig. (4) show the results of CMD simulations, which agree very well with the theoretical predictions. We simulate the field propagation using the Angular Spectrum approach [1] for each point source in the W_a plane, and add the output on an intensity basis. To reduce simulation time, the coherence size at the incoherent source in the simulation was chosen to be 30 μm, which technically makes the source partially coherent. The finite coherence size does cause a slight error in the sidelobes for larger pinhole sizes, but this is too small to be noticed on the graph. Therefore the errors due to propagation and the finite lens aperture are very small, as shown by the good agreement between the CMD simulation and the theoretical curves.

The input coherence width was chosen to be the minimum possible by choosing to maximize the laser spot size on the ground glass. The coherence width without any pinhole was less than 450 μm at the CCD (compared to 1 mm width for the 800 μm pinhole). Note that the Fourier processor has a magnification factor of 5, therefore the width of the input coherence function W_b was less than 100 μm. To predict the coherence functions for partially coherent input fields of arbitrary coherence width, we can consider the following. One can think of the ground glass plane being imaged at the pinhole plane. The pinhole plane then acts as a secondary incoherent source. Then the coherence at the CCD can be found via the van Cittert–Zernike theorem applied to the pinhole plane. Note that this is only an approximation; we are neglecting the finite aperture of the imaging system that relays the ground glass plane to the pinhole plane. In general, the

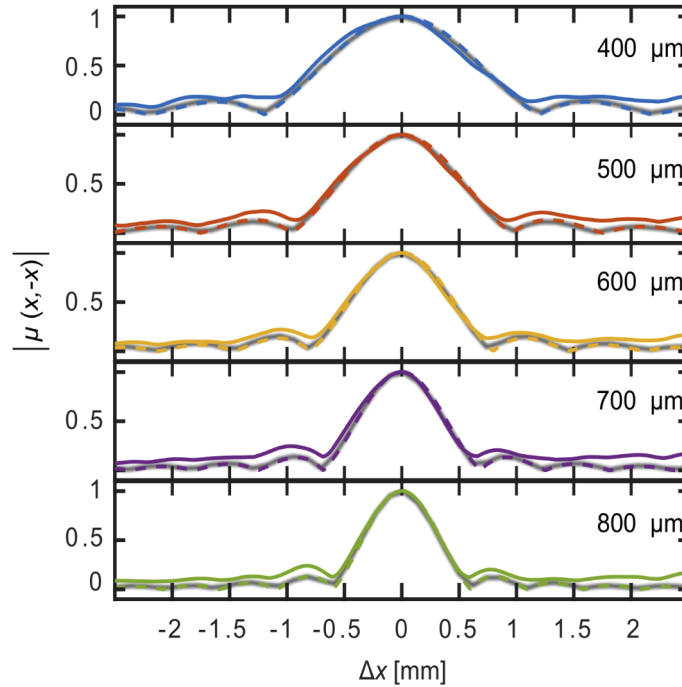field at the pinhole plane will be partially coherent so that the van Cittert–Zernike theorem need not apply.

Fig. 4. Visibility of the horizontal fringes across the horizontal direction for different pinhole diameters. Dashed lines indicate the theoretical predictions of Eq. (1) and Fig. (1), i.e., the coherence curves at the output plane of the $4f$ system. Grey lines are simulated CMD coherence curves after propagation from the $4f$ output to the CCD. For a given pinhole diameter, the experimental coherence values are normalized by the visibility of the central fringe at $x = 0$.

In Fig. (4), the visibility does not drop all the way to zero, because there is always a finite flux from the incident laser that is not scattered from the ground glass. This adds a residual coherence to the beam. We can nevertheless see the coherence sidelobes for each of the pinholes. Slight asymmetry in the curves can be attributed to misalignment and asymmetric vignetting in one of the interferometer arms. Note that experimental factors such as loss of temporal coherence due to the finite laser linewidth or due to unequal path delays in the MZIM, polarization and intensity mismatch from the two arms of the MZIM will reduce the modulation of the coherence globally in x but will not affect the width of the coherence functions. This is evident from the fact that $\mu(x)$ appears as a separate factor in Eq. (3), and the prefactor is independent of x. In particular, loss of temporal coherence will reduce the *local* tilt fringe amplitude due to finite path length difference $k_y|y|>0$, but this reduction of local tilt amplitude should be decoupled from x. Therefore, normalization by the central fringe visibility compensates for reduced temporal coherence.

Other noise effects include CCD noise and pinhole irregularities. The effect of the CCD noise on the measurements is suppressed after background subtraction and averaging over 250 images, where the integration time for each image is 20 ms. The stated tolerance in the pinhole diameters (Thorlabs precision pinholes P400D-P800D, circularity $\geq$ 95 %) is $\pm 10 \mu m$. CMD simulations show that the error due to this slight non-circularity is very small. Figure (5) shows CMD simulation results for the effect of pinhole eccentricity ($e = \sqrt{1 - (a/b)^2}$), where a is the

axis along *x* and *b* is the axis along *y*, on the expected coherence. For an eccentricity of 0.25, the expected coherence curves do not significantly differ from the *e* = 0 case. For *e* = 0.5, which corresponds to *a/b* = 0.86, the sidelobes become larger and the coherence plot becomes narrower compared to the theory curves. Because the stated circularity is ≥ 95%, the actual pinhole eccentricity is much smaller than 0.5. We therefore expect the error from any pinhole irregularities to be small. Further averaging over multiple columns also does not appreciably change the measured coherence curves.
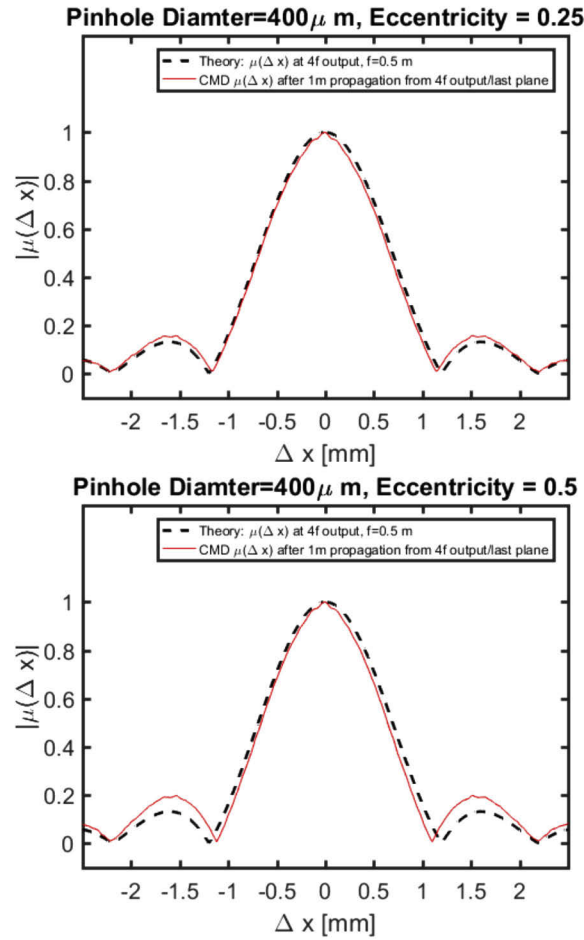

Fig. 5. CMD Simulation results for eccentric pinholes. Dashed lines are theory plots at the 4*f* output for circular pinholes (*e* = 0). Solid lines are expected coherence curves for eccentric pinholes. The solid lines also include propagation effects from the 4*f* output to the CCD.

The upper limit on the tilt angle is set by two parameters: 1) The coherence length of the laser; for better SNR, the highest tilt phase should be less than that corresponding to the laser coherence length. For narrowband light, this constraint is easy to satisfy. 2) CCD Pixel size: The tilt fringe period should be at least Nyquist sampled. Figure (4) therefore demonstrates the Fourier processing of partial coherence, clearly showing the coherence area of the beam decreasing with larger pinhole sizes, as predicted by Fig. (1).

4. Conclusion

In conclusion, we have used spatial filtering in a $4f$ system to control the spatial coherence of a partially coherent beam. The spatial coherence was measured with a MZIM. Our results corroborate the theory presented in [6] and can be used to tailor the coherence properties of beams. Future work can include working with more complicated amplitude and phase masks in the Fourier plane to synthesize arbitrary coherence profile's. This will allow control over the beam's angular and frequency spectrum [5]. The work can also be extended to the control of polarization of partially coherent fields [21].

Disclosures

The authors declare no conflicts of interest.

The codes for CMD are available from the authors upon request.

References

1. J. W. Goodman, *Introduction to Fourier Optics* (Roberts and Company Publishers, 2005).
2. E. Abbe, "Beiträge zur Theorie des mikroskops und der mikroskopischen wahrnehmung," Archiv f. mikrosk. Anatomie **9**(1), 413–468 (1873).
3. A. B. Porter, "XII. On the diffraction theory of microscopic vision," London Edinburgh Philos. Mag. J. Sci. London **11**(61), 154–166 (1906).
4. J. W. Goodman, *Statistical Optics* (John Wiley & Sons, 2015).
5. L. Mandel and E. Wolf, *Optical Coherence and Quantum Optics* (Cambridge University Press, 1995).
6. T. D. Visser, G. P. Agrawal, and P. W. Milonni, "Fourier processing with partially coherent fields," Opt. Lett. **42**(22), 4600–4602 (2017).
7. F. Wang, X. Liu, Y. Yuan, and Y. Cai, "Experimental generation of partially coherent beams with different complex degrees of coherence," Opt. Lett. **38**(11), 1814–1816 (2013).
8. B. Rodenburg, M. Mirhosseini, O. S. Magaña-Loaiza, and R. W. Boyd, "Experimental generation of an optical field with arbitrary spatial coherence properties," J. Opt. Soc. Am. B **31**(6), A51–A55 (2014).
9. J. Lehtolahti, M. Kuittinen, J. Turunen, and J. Tervo, "Coherence modulation by deterministic rotating diffusers," Opt. Express **23**(8), 10453–10466 (2015).
10. X. Chen, J. Li, S. M. H. Rafsanjani, and O. Korotkova, "Synthesis of Im-Bessel correlated beams via coherent modes," Opt. Lett. **43**(15), 3590–3593 (2018).
11. X. Liu, D. Xia, Y. E. Monfared, C. Liang, F. Wang, Y. Cai, and P. Ma, "Generation of novel partially coherent truncated airy beams via fourier phase processing," Opt. Express **28**(7), 9777–9785 (2020).
12. T. Wu, C. Liang, F. Wang, and Y. Cai, "Shaping the intensity and degree of coherence of a partially coherent beam by a 4f optical system with an amplitude filter," J. Opt. **19**(12), 124010 (2017).
13. C. Mi, C. Liang, F. Wang, L. Liu, Y. Gao, and Y. Cai, "Modulating the statistical properties of a vector partially coherent beam by a 4f optical system," J. Quant. Spectrosc. Radiat. Transfer **222-223**, 145–153 (2019).
14. H. Sasada and M. Okamoto, "Transverse-mode beam splitter of a light beam and its application to quantum cryptography," Phys. Rev. A **68**(1), 012323 (2003).
15. J. B. Breckinridge, "Coherence interferometer and astronomical applications," Appl. Opt. **11**(12), 2996_1–2998 (1972).
16. M. Santarsiero and R. Borghi, "Measuring spatial coherence by using a reversed-wavefront young interferometer," Opt. Lett. **31**(7), 861–863 (2006).
17. D. P. Brown and T. G. Brown, "Partially correlated azimuthal vortex illumination: coherence and correlation measurements and effects in imaging," Opt. Express **16**(25), 20418–20426 (2008).
18. J. W. Goodman, *Speckle Phenomena in Optics: Theory and Applications* (Roberts and Company Publishers, 2007).
19. W. Martienssen and E. Spiller, "Coherence and fluctuations in light beams," Am. J. Phys. **32**(12), 919–926 (1964).
20. E. Wolf, "New spectral representation of random sources and of the partially coherent fields that they generate," Opt. Commun. **38**(1), 3–6 (1981).

21. X. Zhao, T. D. Visser, and G. P. Agrawal, "Controlling the degree of polarization of partially coherent electromagnetic beams with lenses," Opt. Lett. **43**(10), 2344–2347 (2018).